Chemical Science

ROYAL SOCIETY OF CHEMISTRY

EDGE ARTICLE

View Article Online
View Journal | View Issue

Cite this: *Chem. Sci.*, 2025, **16**, 7077

All publication charges for this article have been paid for by the Royal Society of Chemistry

An intramolecularly locked single molecule nanofluorophore with 13.55% quantum yield for SWIR multimodal phototheranostics†

Leilei Si,[abc] Jun Tang,[abc] Kaixin Yang,[abc] Mingda Wang,[abc] Yigang Wang,[bc] Guomin Xia *[bcd] and Hongming Wang *[ab]

Received 6th January 2025
Accepted 11th March 2025

DOI: 10.1039/d5sc00089k

rsc.li/chemical-science

Multimodal phototheranostics in the short-wavelength infrared range (SWIR, 900–1700 nm) holds significant promise in precision medicine, yet its progress is constrained by photosensitizers that lack effective fluorescence emission due to unwanted intermolecular aggregation and molecular vibration patterns. Herein, we present a dual electrostatic anchoring strategy to construct ultrabright co-assembled nanoparticles (NPs) of the squaraine dye SQNMe. This molecular design incorporates two peripheral quaternary ammonium cations: one interacts with the phosphate anion of the liposome $mPEG_{2K}$-DSPE to achieve intermolecular isolation, while the other forms an internal salt bridge with the central oxycyclobutenolate ring, increasing intramolecular rigidity. Both molecular dynamics simulations and reorganization energy calculations are employed to illustrate the coassembly process. Spectroscopic analysis shows that SQNMe@NPs have a fluorescence brightness of approximately 10 135 M^{-1} cm^{-1} and a photothermal conversion efficiency of 39.6% in aqueous media. Additionally, the high effectiveness of fluorescence and photoacoustic imaging-guided photothermal therapy for tumors *in vivo* was successfully demonstrated. These findings highlight the potential of the electrostatic anchoring strategy for improving multimodal tumor phototheranostics.

Introduction

Multimodal phototheranostics is emerging as a vital approach in precision medicine.[1–5] The innovative integration of diverse modalities can overcome individual limitations and harness their combined advantages, leading to enhanced therapeutic outcomes.[6–10] This approach is particularly relevant in the short-wave infrared (SWIR, 900–1700 nm), which offers superior tissue penetration, minimal scattering, and reduced autofluorescence.[11–16] As an important category of photosensitizers, the low-bandgap organic small molecules often exhibit a guaranteed photothermal effect with poor fluorescence efficiency in the SWIR range.[17–21] This is ascribed to the rapid nonradiative relaxation of molecules in excited states upon photoinitiation *via* the $S_n \rightarrow S_0$ internal conversion process, which is primarily caused by intramolecular vibrations.[22,23] The issue is exacerbated in their aggregated state, where additional nonradiative relaxation pathways arise from intermolecular interactions, such as charge transfer or a reduction in the transition dipole moment in face-to-face stacked H-aggregates.[24–28] Therefore, enhancing the fluorescence efficiency of these low-bandgap dye molecules is crucial for the effectiveness of multimodal phototheranostics.

It is now routine to encapsulate dye molecules in liposomes to achieve biological advantages, such as high biocompatibility, prolonged blood circulation, and enhanced tumor retention, in phototheranostics.[29–36] However, this often results in the encapsulated dye molecules being in an uncontrollable aggregated state at the center of the nanostructures, making the pathways for its excited state energy dissipation difficult to ascertain and thus challenging to manipulate further.[37–39] Although efficient SWIR fluorescent emission from aggregated states, such as aggregation-induced emission luminogens (AIEgens)[40–42] and J-aggregates,[43–45] can be achieved by customizing the molecular skeletons within these nanostructures, the existing molecular archetypes are limited, and a universal design principle has yet to be established. For this, researchers have focused on introducing electrostatic interactions between phosphate anions in liposomes and dye molecules with incorporating side-chain cations. This electrostatic interaction anchors the dye molecules in a monodisperse form within the lipid layer, avoiding complex aggregation and improving fluorescence efficiency.[39,46–50] Nevertheless, their fluorescence

[a]*College of Chemistry and Chemical Engineering, Nanchang University, Nanchang 330031, China. E-mail: hongmingwang@ncu.edu.cn*

[b]*Jiangxi Provincial Key Laboratory of Functional Crystalline Materials Chemistry, Nanchang 330031, China. E-mail: guominxia@ncu.edu.cn*

[c]*Institute for Advanced Study, Nanchang University, Nanchang 330031, China*

[d]*School of Advanced Manufacturing, Nanchang University, Nanchang 330031, China*

† Electronic supplementary information (ESI) available. See DOI: https://doi.org/10.1039/d5sc00089k

brightness, which remains below 500 M^{-1} cm^{-1}, is considered unsatisfactory in multimodal phototheranostics (for details see Table S1†).

It is reasonable to conjecture that molecular vibrations are the primary factor contributing to the suboptimal efficiency of these monodispersed photosensitizers within the soft lipid layer (top in Fig. 1). In this context, our objective is to develop a strategy that addresses the challenges posed by unwanted intermolecular aggregation while minimizing the detrimental effects of intramolecular vibrations. To achieve this, we designed and synthesized a bicationic squaraine dye, SQNMe, featuring a propyl-based quaternary ammonium group at each peripheral side chain. Through co-assembly with the liposome $mPEG_{2K}$-DSPE, stable nanoaggregates are formed, incorporating two types of electrostatic interactions that allow the salt bridge-rigidified SQNMe to disperse as single molecules within the lipid layer. These unified nanofluorophores exhibit ultrahigh SWIR fluorescence brightness, suitable photothermal conversion efficiency (PCE), and excellent biocompatibility and biosafety, positioning them as outstanding candidates for multimodal phototheranostic applications (bottom of Fig. 1).

Results and discussion

We initiated this investigation by conceptualizing dicationic SWIR squaraine dyes as target candidates for multimodal phototheranostics, inspired by previous literature.[51,52] To begin with, a propyl-based quaternary ammonium was introduced into benzo[*cd*]indol-2(1*H*)-one, followed by methylation and subsequent condensation with squaric acid to yield the desired dye molecule, SQNMe. The compounds involved in the synthesis steps were characterized using ^{1}H NMR, ^{13}C NMR, and high-resolution mass spectrometry (for details see the ESI†). By examining the absorption spectra of SQNMe, we observed that the maximum absorption peak (λ_{ab}) in dimethyl sulfoxide (DMSO) is at 892 nm, with a shoulder peak at 800 nm. In contrast, these values in pure water (H_2O) were detected at 738 nm and 832 nm, with a slight drop in absorbance (Fig. S1†). This blue shift in the absorption spectra indicates the formation

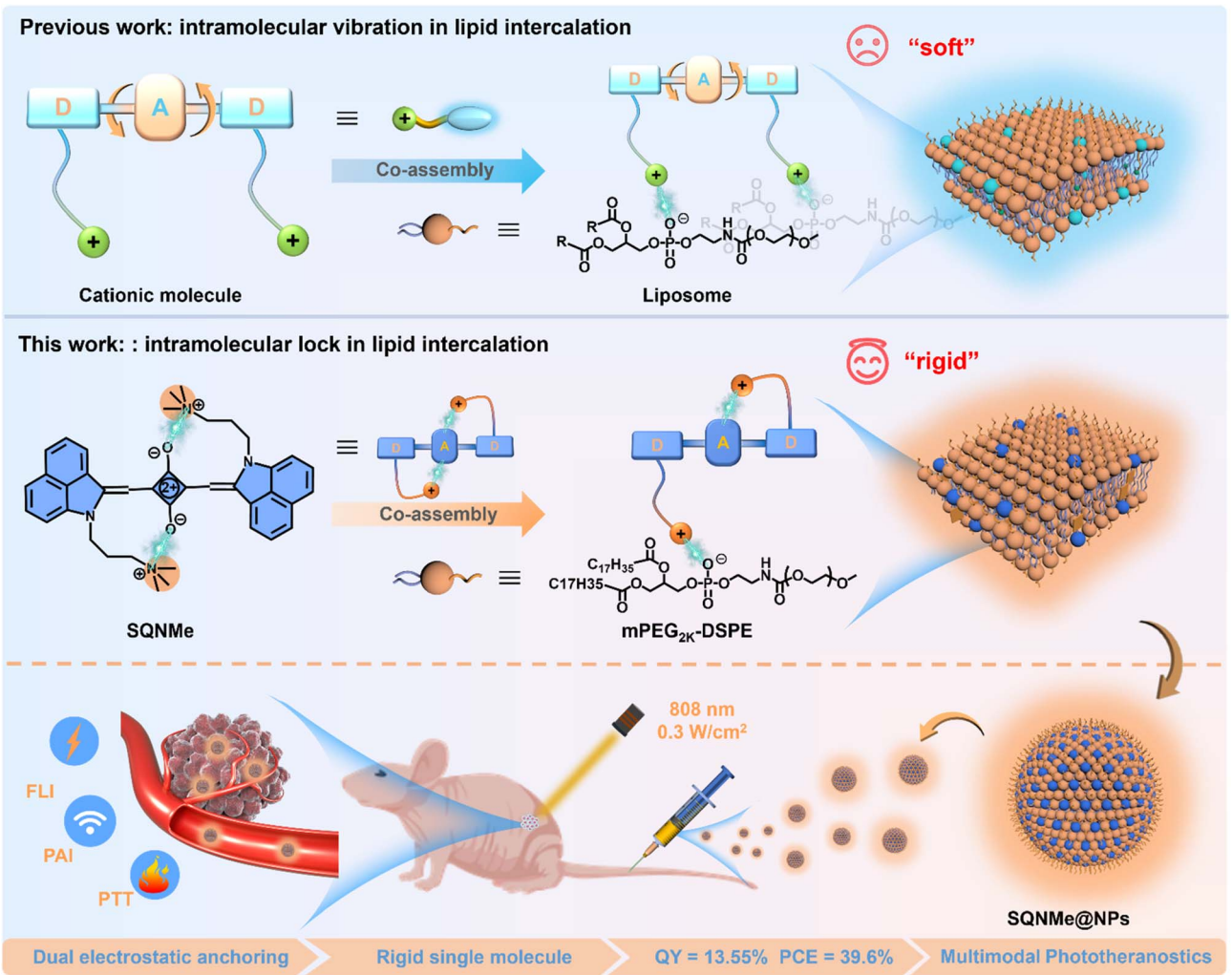

Fig. 1 Molecular vibrations in the soft lipid layer likely limit the efficiency of single molecule photosensitizers (top); unified nanofluorophores exhibit ultrahigh SWIR fluorescence, efficient photothermal conversion, and excellent biocompatibility, making them ideal for multimodal phototheranostics (bottom).

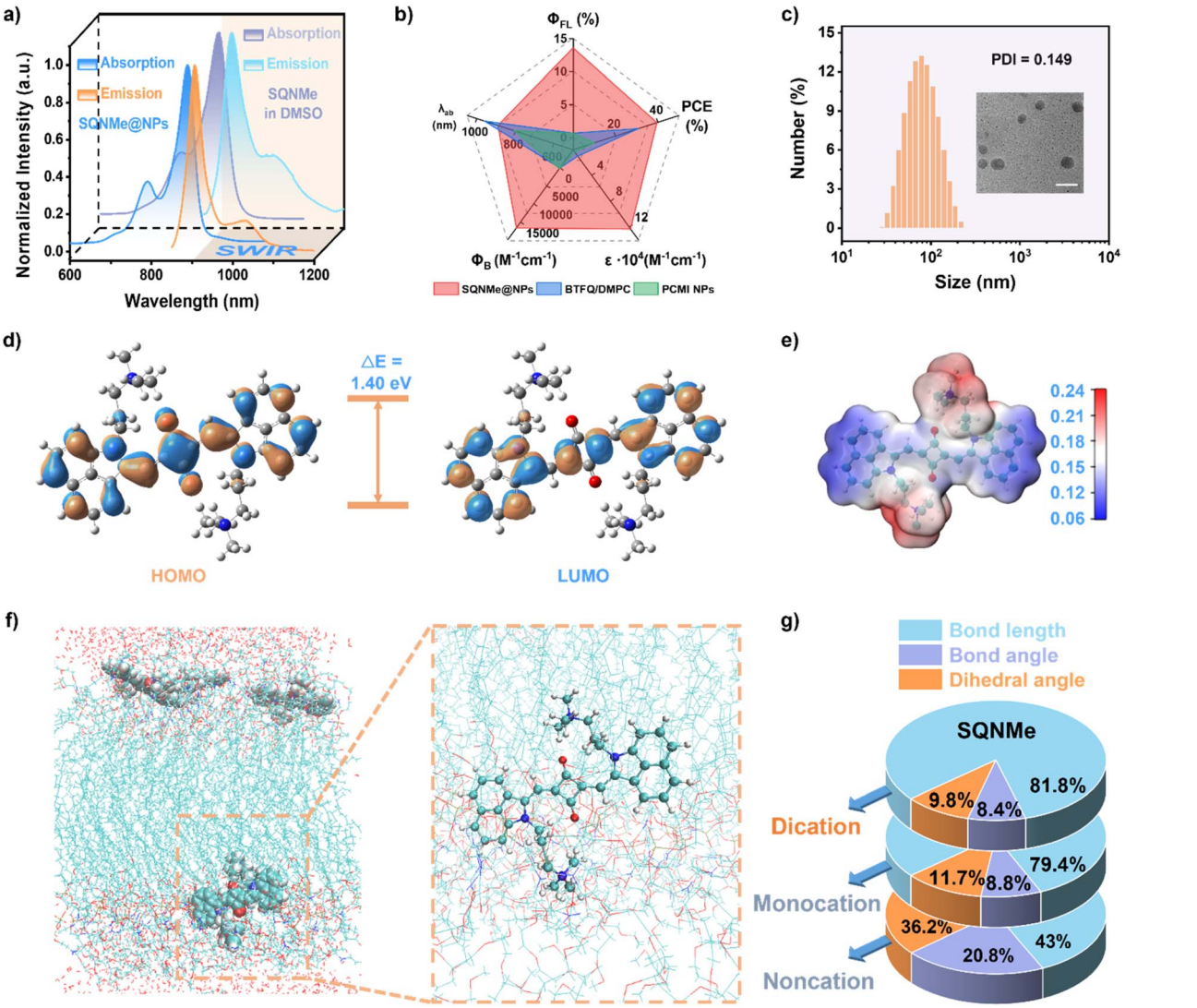

Fig. 2 (a) Normalized absorption and emission spectra of SQNMe@NPs and SQNMe in DMSO; (b) radar chart illustrating the photophysical properties of SQNMe@NPs compared to analogous nanoparticles prepared *via* electrostatic anchoring; (c) dynamic light scattering analysis of prepared SQNMe@NPs, along with their photographs and TEM images in water (scale bar: 200 nm); (d) DFT-optimized structures of SQNMe showing HOMO and LUMO distributions; (e) electrostatic potential map of SQNMe; (f) molecular dynamics simulation of SQNMe in liposomes; (g) contributions to the total reorganization energy from dihedral angle, bond length, and bond angle.

of H-aggregation modes of SQNMe in H_2O, consistent with our previous literature.[53]

Using a nanoprecipitation method, the coassembly process of oppositely charged SQNMe and the liposome $mPEG_{2k}$-DSPE was then examined in an aqueous medium (for details see the ESI†). We named these nanoparticles SQNMe@NPs. As shown in Fig. S2,† an increase in the molar ratio of $mPEG_{2k}$-DSPE to SQNMe results in a redshift in the absorption spectrum of the resulting SQNMe@NPs. Specifically, its absorption peak at 738 nm gradually decreases, while the peak at 890 nm increases, stabilizing at a ratio of 20 : 1. This optimal absorption spectrum of SQNMe@NPs closely matches that of SQNMe in DMSO (Fig. S3†), indicating a transformation from H-aggregates to a dispersed state with the addition of $mPEG_{2k}$-DSPE. Thus, it is reasonable to conjecture that SQNMe exists as a single molecule within the liposome interlayer of SQNMe@NPs due to electrostatic interactions.

Following the optimal ratio, SQNMe@NPs were then prepared and subjected to dialysis for subsequent experiments. From concentration dependent absorption spectra, the entrapment efficiency for SQNMe@NPs was determined to be 62.86% (Fig. S4†). As shown in Fig. 2a, the absorption peak of fresh SQNMe@NPs is at 890 nm, with a shoulder peak at 800 nm. The maximum emission peak (λ_{em}) is at 906 nm, accompanied by a shoulder peak at 1032 nm that extends up to 1100 nm. The axisymmetric relationship between the absorption and emission spectra, along with their similarity to the spectra of SQNMe in DMSO, indicates that SQNMe exists as a single molecule in the nanoparticles and undergoes no significant structural changes in its excited state upon photon

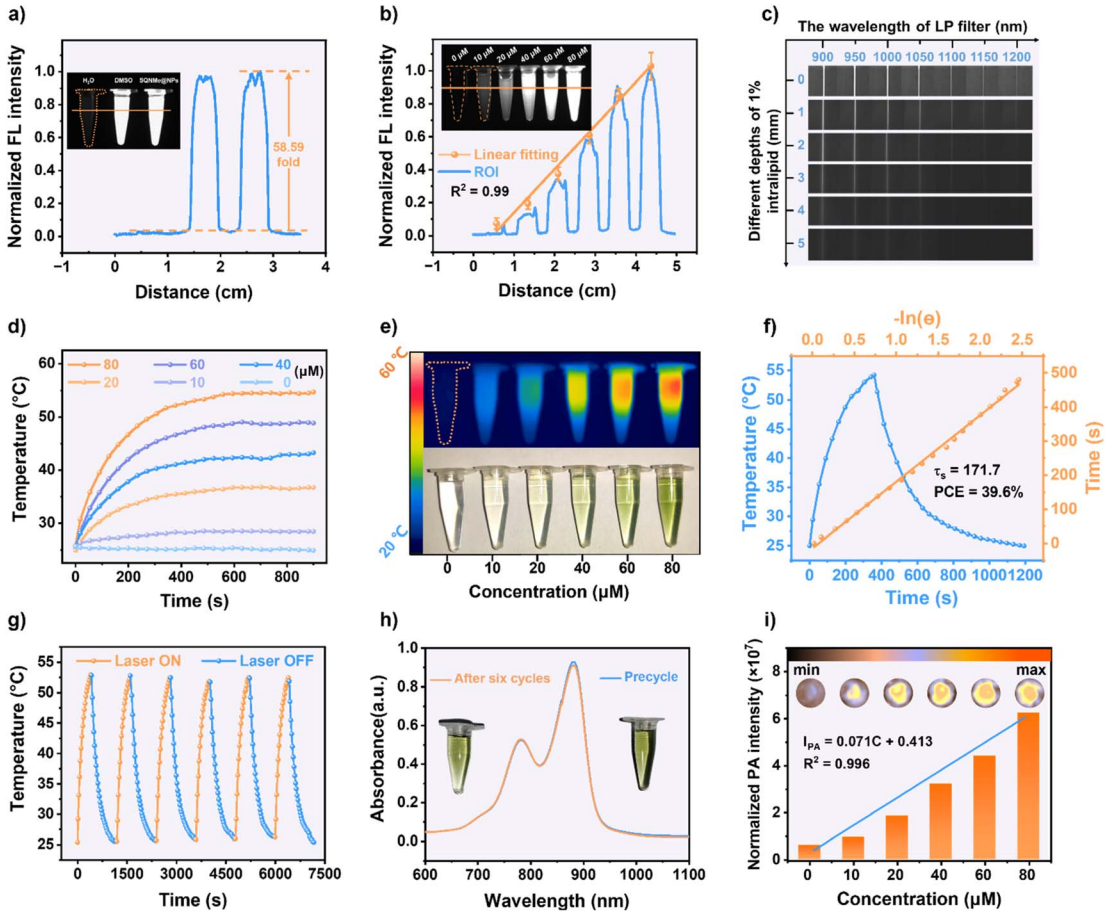

Fig. 3 (a) NIR-II fluorescence imaging and intensity distributions of SQNMe, DMSO, and SQNMe@NPs at 80 μM; (b) intensity distributions and linear fitting for SQNMe@NPs at different concentrations; (c) penetration depth imaging of SQNMe@NPs in fat emulsion solution; (d) heating curves and (e) corresponding thermal imaging for SQNMe@NPs at different concentrations; (f) cooling curves and their linear correlation with temperature; (g) six cycles of heating and cooling curves of SQNMe@NPs and (h) absorption spectra before and after cycling; (i) *in vitro* PA intensity and imaging of SQNMe@NPs at different concentrations.

excitation. Using ICG as a reference standard, the fluorescence quantum yield (Φ_{FL}) of SQNMe@NPs was measured at 13.55%. With a molar absorption coefficient of 1.2×10^5 M^{-1} cm^{-1}, the resulting fluorescence brightness was approximately 10 135 M^{-1} cm^{-1} (Fig. S5†). These values are considerably higher than those of nanoparticles synthesized using the same electrostatic anchoring strategy (see Table S1† and Fig. 2b), as well as compared to other types of nanofluorophores (Table S2†). Laser irradiation of SQNMe@NPs, followed by the use of 2′,7′-dichlorofluorescin diacetate (H2DCFHDA) indicator, showed negligible generation of reactive oxygen species (Fig. S6†).

Subsequently, dynamic light scattering (DLS) analysis indicated that the SQNMe@NPs had a dynamic diameter of approximately 98 nm, with a polydispersity Index (PDI) of 0.149 (Fig. 2c). These findings align with the results from transmission electron microscopy (TEM) and suggest that the particles are well-suited for *in vivo* enrichment through the enhanced permeability and retention (EPR) effect in tumors.[54,55] Additionally, the zeta potential measurement of SQNMe@NPs revealed a value of −32.5 mV (Fig. S7†). Stability tests conducted in various media (PBS, 0.9% NaCl, RPMI-1640) on the 1st, 7th, and 15th days showed no significant changes in the absorbance spectra of SQNMe@NPs. Both the particle size and zeta potential also remained unchanged, further indicating the robust chemical stability of SQNMe@NPs (Fig. S8†).

To gain further insights, molecular dynamics simulations (MDS, for details see the ESI†) were employed to model the co-assembly process of SQNMe with the liposome $mPEG_{2k}$-DSPE. The structure of the SQNMe molecule was initially optimized, revealing excellent molecular planarity, with the cationic nitrogen atoms of the ammonium salts bridged by the central oxygen atom. The distances were 3.46 Å and 3.29 Å, which aligns well with the effective range for electrostatic interactions (Fig. S9†). Theoretical calculations revealed that the highest occupied molecular orbital (HOMO) is predominantly delocalized across the conjugated backbone, while the lowest unoccupied molecular orbital (LUMO) was mainly confined to the donor region (Fig. 2d). This specific distribution of molecular orbitals, featuring a peripheral "salt bridge," facilitate the rigidity of the whole molecule, effectively suppressing vibrational non-radiative transitions in its excited state (Fig. 2e). The

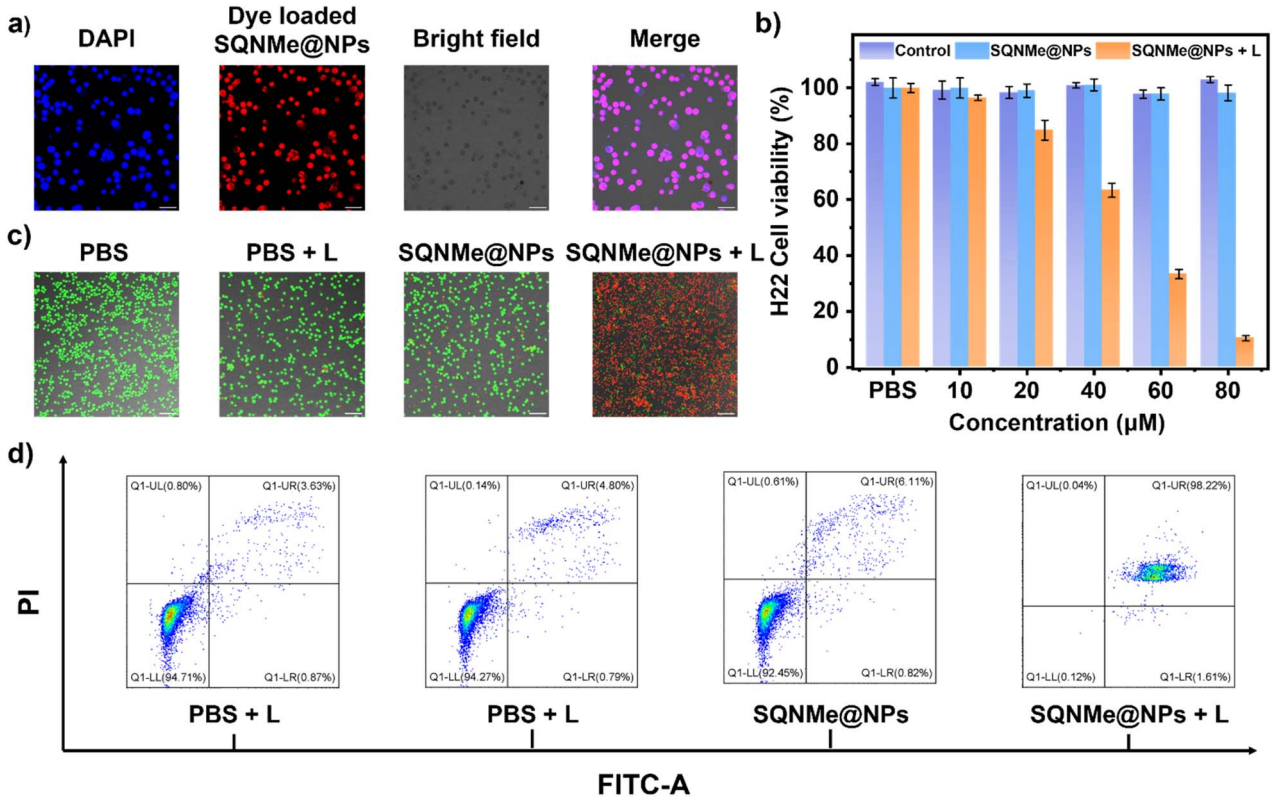

Fig. 4 (a) Cell phagocytosis experiment. Confocal laser scanning microscope images showing DAPI (blue) and SQNMe@NPs @ dye (red) (scale bars, 50 μm). (b) Evaluation of cell viability of H22 cells treated with different concentrations using the MTT assay. Error bars represent mean ± SD ($n = 3$). (c) Viability staining experiment of H22 cells under different treatment conditions (scale bars, 100 μm). (d) Flow cytometry experiment of H22 cells under different treatment conditions.

calculated band gap of 1.40 eV was also in excellent agreement with experimental data (Fig. S10†).

A simplified mPEG-DSPE model was subsequently constructed in water, followed by a 60 ns molecular dynamics simulation. The results revealed that four SQNMe molecules predominantly existed as single molecule, positioned between the phosphate groups and alkyl chains of the liposome (Fig. 2f). It is worth mentioning that only one quaternary ammonium group of SQNMe functions as an "anchor" to embed itself into the hydrophilic region of the liposome *via* electrostatic interactions. The other one keep the electrostatic interactions with the central oxygen atom, reinforces its structural rigidity. This reasoning is well-founded, as anchoring the hydrophilic ammonium groups on opposite sides entirely with phosphate anions would inevitably result in significant structural changes, contradicting the observed spectral data. Additionally, reorganization energy analysis reveals that molecules with cationic salt bridges exhibit a lower total reorganization energy (Fig. S11†). When projected onto the corresponding internal coordinates, the analysis reveals that reorganization in the excited state is primarily driven by bond-length stretching, resulting in rearrangement. This suggests that molecular reorganization in the excited state is predominantly driven by stretching vibrations, with the cationic salt bridge stabilizing the molecular structure and enhancing its rigidity (Fig. 2g).

For comparison, we also prepared nanoparticles of the salt-bridge-free molecule SQEt, referred to as SQEt@NPs (see ESI† for details). The Φ_{FL} of SQEt@NPs was found to be 20 times lower than that of SQNMe@NPs (Fig. S5†), further highlighting the crucial role of the electrostatic anchoring strategy.

Using an 808 nm laser (0.3 W cm^{-2}), fluorescence images were captured with an InGaAs camera. The results showed no detectable signal for SQNMe in H_2O, whereas significant signal brightness was observed in the other two solutions (Fig. 3a). These observations align with the fluorescence-quenching effect of H-aggregation in SQNMe within H_2O, whereas a monodispersed, fluorescence-emitting single state is consistently formed in both DMSO and nanostructures. Additionally, they highlight the unique advantage of electrostatic interactions, which prove beneficial compared to traditional non-covalent interactions, such as dispersion forces and the antiparallel alignment of ground-state dipoles. Notably, there is a linear correlation between the concentration of SQNMe@NPs and signal brightness (Fig. 3b), with the correlation coefficient of 0.99. The permeability test in lipid emulsion solutions demonstrated that even after passing through a 1000 nm long-pass filter, the depth of penetration exceeded 3 mm (Fig. 3c). All these results indicate that SQNMe@NPs exhibits potentially superior fluorescence imaging capabilities *in vivo*.

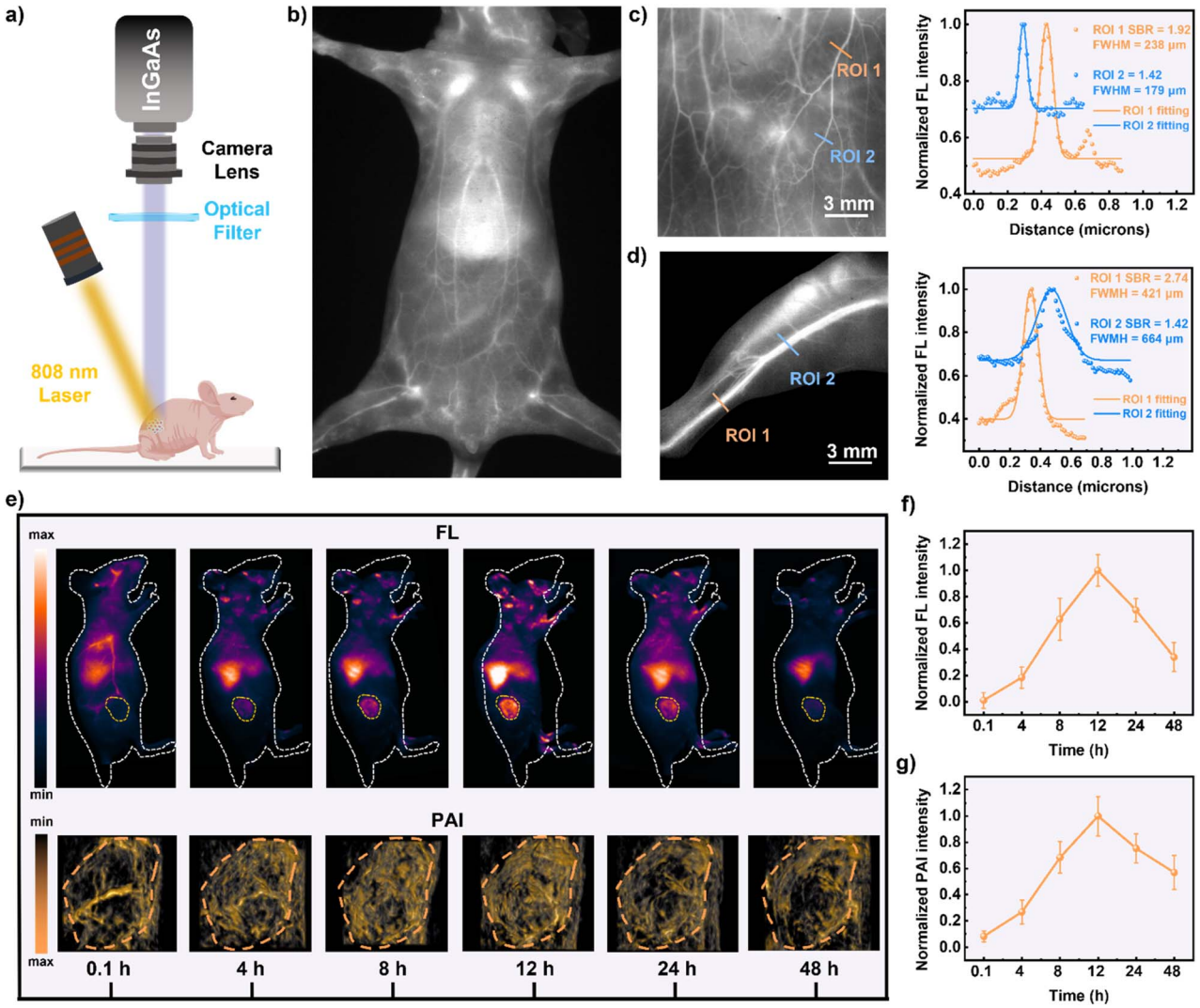

Fig. 5 (a) Schematic diagram of *in vivo* fluorescence imaging captured by an InGaAs camera; (b) *in vivo* near-infrared fluorescence vascular imaging of mice. (c) Fluorescence images of the abdomen and (d) lower limbs of mice after intravenous injection of SQNMe@NPs (200 μM, 200 μL), with corresponding intensity distribution plots of solid cross-sections on the right; (e) tumor accumulation of SQNMe@NPs in H22 tumor-bearing mice at different time points after intravenous injection, where FLI and PAI represent fluorescence imaging and photoacoustic imaging, respectively; (f) fluorescence signal intensity and (g) photoacoustic signal intensity at different time points after intravenous injection (error bars represent mean ± SD ($n = 3$)). The fluorescence imaging conditions were set as follows: 808 nm excitation, laser power density of 0.3 W cm^{-2}, a 1000 nm long-pass filter, and an exposure time of 100 ms. The concentration of all intravenously injected SQNMe@NPs is 200 μM, with a volume of 200 μL.

Next, the temperature increase from varying concentrations of SQNMe@NPs (0–80 μM) was monitored, and the peak temperature was captured using infrared cameras. Upon laser irradiation (808 nm, 0.3 W cm^{-2}), SQNMe@NPs reached a stable peak temperature up to 54.7 °C within 6 min, corresponding to an approximate temperature increase (ΔT) of 30 °C. These results for SQNMe@NPs demonstrated a concentration-dependent increase in temperature, and the PCE of SQNMe@NPs was calculated to be 39.6% (Fig. 3d–f and S12†), making *in vivo* PTT feasible. In contrast, the PCE of H-aggregated SQNMe in H_2O was measured at 59.8% (Fig. S13 and S14†), which is close to the 64.25% observed for SQEt@NPs. These findings are consistent with the calculated results, indicating that the dual electrostatic anchoring strategy facilitates radiative decay (Fig. S14†). Over six cycles of laser-induced heating and cooling, SQNMe@NPs exhibited minimal changes in temperature elevation (Fig. 3g and S15†), and the nearly unchanged absorption spectra indicate that SQNMe@NPs possess excellent photostability and thermal stability (Fig. 3h). Additionally, the photoacoustic test revealed a positive correlation between signal intensity and concentration of SQNMe@NPs (Fig. 3i), establishing a foundation for *in vivo* photoacoustic imaging (PAI).

As shown in Fig. 4a, co-incubation of red-emitting dye-loaded SQNMe@NPs with H22 cells resulted in co-localization with DAPI, indicating successful cellular uptake.[56] The light

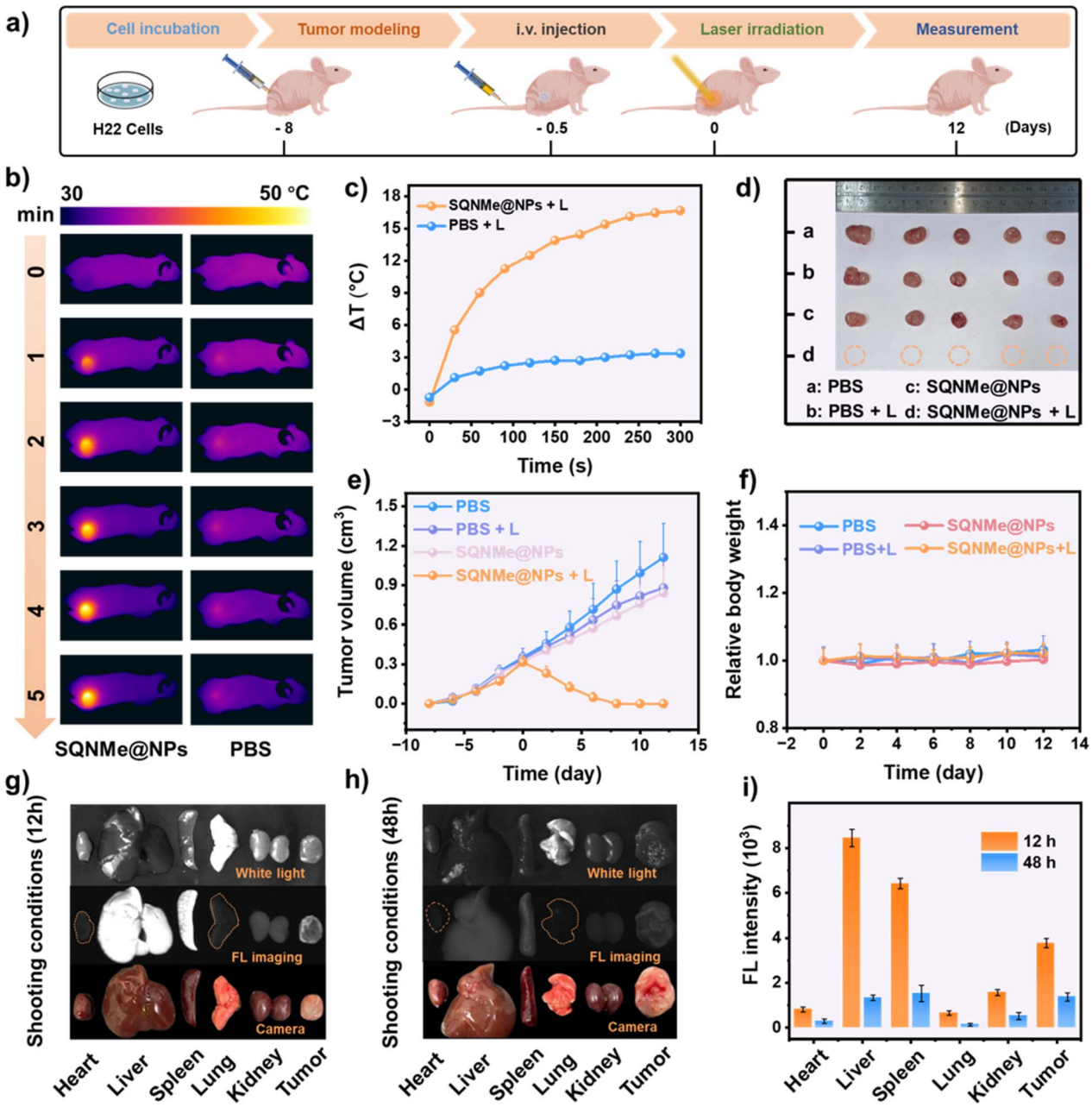

Fig. 6 (a) Schematic diagram of *in vivo* experiments in mice. (b) Temperature elevation images of H22 tumor-bearing mice treated with PBS and SQNMe NPs under laser irradiation (808 nm, 0.3 W cm^{-2}) for 10 minutes, and (c) relative temperature elevation curve at the tumor site. (d) Images of excised tumors from different treatment groups. (e) Tumor volume changes during treatment in different treatment groups, and (f) changes in mouse body weight; images of isolated organs and tumors from mice at (g) 12 h and (h) 48 h post-injection, along with (i) the corresponding fluorescence intensity profiles of major organs and tumor sites.

cytotoxicity of the SQNMe@NPs was then assessed using MTT assays. H22 cell viability in the SQNMe@NPs group was comparable to that of the control group without laser irradiation, suggesting good biocompatibility (Fig. 4b). Upon laser irradiation, H22 cell viability decreased with increasing SQNMe@NPs concentration, dropping to around 10% at 80 μM, due to the photothermal effect of SQNMe@NPs. Furthermore, live/dead staining assay observations were consistent with the results, and further confirmed by the subsequent flow cytometry (Fig. 4c and d).

The multimodal imaging performances of SQNMe@NPs were then evaluated through *in vivo* experiments. Intravenous administration of SQNMe@NPs enabled live vascular fluorescence imaging in the macromodel, revealing clear and detailed vascular structures (Fig. 5b). The vessel width and signal-to-background ratio (SBR) were measured and calculated by Gaussian fitting of the cross-sectional fluorescence intensity

profile and calculating its full width at half-maximum (FWHM). From the micromodel, the fluorescence images of the mice's hind limbs achieved a peak SBR of 2.74, while the abdomen reached a maximum SBR of 1.92 (Fig. 5c and d). The FWHM of the hindlimb vessels measured along the solid line were 421 and 664 μm, respectively (Fig. 5c). Similarly, the widths of the abdominal vessels were 238 and 179 μm, respectively (Fig. 5d). Subsequently, SQNMe@NPs were administered intravenously to tumor-bearing mice, and fluorescence and photoacoustic imaging were performed at various time points. As shown in Fig. 5e (upper part), the signal intensity at the tumor site progressively increased over time, peaking at 12 hours before gradually declining and nearly disappearing by 48 hours. This pattern can be attributed to the accumulation of SQNMe@NPs in the tumor region *via* the EPR effect, along with simultaneous biological clearance within 48 hours. Additionally, the time-dependent photoacoustic signal results for the tumor were consistent with those from fluorescence imaging (Fig. 5e bottom part, Fig. S16†), indicating the potential for SWIR fluorescence imaging-guided photothermal therapy starting 12 hours post-injection (Fig. 5f and g).

The schematic of the multimodal tumor phototheranostics process over the 21 day period is depicted in Fig. 6a. Twelve hours after injection, the intratumoral temperature elevation of SQNMe@NPs was monitored using an infrared camera, as shown in Fig. 6b. Within 5 minutes of laser exposure, a significant increase of 18 °C in tumor temperature was observed in mice injected with SQNMe@NPs, while minimal change (less than 3 °C) was noted in mice injected with PBS (Fig. 6c). This temperature increase from SQNMe@NPs is sufficient to facilitate photothermal therapy (PTT) for tumor ablation.

Subsequently, we divided the mice with a tumor volume of 0.3 cm^3 into four groups: PBS, PBS + L, SQNMe@NPs, and SQNMe@NPs + L. After 24 hours post-treatment, tumor tissues were extracted. Tissue sections showed irregularities in the nuclear shape of H22 cells in the SQNMe@NPs + L group, along with notable changes in cell morphology compared to the other three groups, suggesting the occurrence of cellular necrosis (Fig. S17†). As shown in Fig. 6d, complete tumor ablation was observed in the SQNMe@NPs + L group. This process is captured in Fig. S18,† indicating the strong photothermal capability of SQNMe@NPs. Additionally, the tumor volume recording curves of the mice aligned well with the experimental results (Fig. 6e). During the treatment period, the mice's body weight showed no significant changes, indicating the absence of adverse effects associated with SQNMe@NPs (Fig. 6f).

Following the administration of SQNMe@NPs, we conducted dissections of tumor-bearing mice at both 12 and 48 hours post-injection. Examination of the major organs revealed no apparent abnormalities. Results indicated that the drug primarily underwent metabolism in the liver and spleen, with a decrease of 84.12% in signal intensity associated with the liver after 48 hours (refer to Fig. 6g–i), suggesting excellent biodegradability of SQNMe@NPs. Furthermore, routine blood tests during treatment revealed no abnormalities in liver, kidney, or immune function, and there were no discernible signs of inflammation or infection (Fig. S19†). Histological analysis post-treatment showed no significant organ abnormalities or inflammation (Fig. S20†). All these findings confirm the effectiveness and biosafety of our dual electrostatic anchoring strategy in achieving SWIR multimodal phototheranostics.

Conclusion

In summary, we demonstrated an anchoring strategy to construct ultrabright nanoaggregates SQNMe@NPs, incorporating two types of electrostatic interactions that enable the salt bridge-rigidified SQNMe to disperse as single molecules within the lipid layer. This archetype is supported by molecular dynamics simulations and reorganization energy calculations. Thus, the ultrabrightness of SQNMe@NPs was calculated up to approximately 10 135 M^{-1} cm^{-1} and a PCE of 39.6% in aqueous media, permitting successful fluorescence and photoacoustic imaging-guided PTT for tumors *in vivo*. These findings underscore the promise of the electrostatic anchoring strategy in advancing multimodal tumor phototheranostics, paving the way for enhanced therapeutic efficacy and precision in cancer treatment.

Ethical statement

All animal experiments were conducted in strict accordance with the management and technical specifications outlined by Nanchang University. The study received ethical approval from the Animal Ethics Committee of Nanchang University under the approval number NCULAE-20230610005.

Data availability

Data will be made available on request.

Author contributions

H. W. and G. X. conceived and designed the experiments for this project. L. S. performed the synthetic work, while L. S., Y. W., and K. Y. carried out the characterization of the compounds. L. S., Y. W., and J. T. also contributed to the photophysical experiments. Data analysis was conducted by H. W., G. X., and L. S. Additionally, H. W. and M. W performed the quantum-chemical calculations. H. W., G. X., and L. S. prepared the initial manuscript, with all other authors contributing to revisions. All authors discussed the results and provided feedback on the manuscript.

Conflicts of interest

There are no conflicts to declare.

Acknowledgements

This work was supported by the National Natural Science Foundation of China (No. 22063005, No. 22465023), the Natural Science Foundation of Jiangxi Province (No. 20212ACBA203012, 20224BAB214003, 20232BAB203031), the Interdisciplinary

Innovation Fund of Natural Science at Nanchang University (No. 9167-27060003-ZD2101, 9167-28220007-YB2113), and the Foundation of Jiangxi Provincial Key Laboratory of Functional Crystalline Materials Chemistry (No. 2024SSY05162). The authors would like to thank Yingzhong Li for his valuable contributions to the molecular synthesis.

Notes and references

1 K. Welsher, Z. Liu, S. P. Sherlock, J. T. Robinson, Z. Chen, D. Daranciang and H. Dai, *Nat. Nanotechnol.*, 2009, **4**, 773–780.
2 A. L. Antaris, H. Chen, K. Cheng, Y. Sun, G. Hong, C. Qu, S. Diao, Z. Deng, X. Hu, B. Zhang, X. Zhang, O. K. Yaghi, Z. R. Alamparambil, X. Hong, Z. Cheng and H. Dai, *Nat. Mater.*, 2015, **15**, 235–242.
3 Z. Li, B. Z. Tang and D. Wang, *Adv. Mater.*, 2024, **36**, 2406047.
4 Y. Chen, S. Wang and F. Zhang, *Nat. Rev. Bioeng.*, 2023, **1**, 60–78.
5 W.-G. Qiao, T. Ma, S. Wang, L. Li, M. Liu, H. Jiang, Y. Wu, J. Zhu and Z. Li, *Adv. Funct. Mater.*, 2021, **31**, 2105452.
6 C. Lu, C. Meng, Y. Li, J. Yuan, X. Ren, L. Gao, D. Su, K. Cao, M. Cui, Q. Yuan and X. Gao, *Nat. Commun.*, 2024, **15**, 5000.
7 S. Song, Y. Zhao, M. Kang, F. Zhang, Q. Wu, N. Niu, H. Yang, H. Wen, S. Fu, X. Li, Z. Zhang, B. Z. Tang and D. Wang, *Adv. Mater.*, 2024, **36**, 2309748.
8 B. Li, W. Wang, L. Zhao, D. Yan, X. Li, Q. Gao, J. Zheng, S. Zhou, S. Lai, Y. Feng, J. Zhang, H. Jiang, C. Long, W. Gan, X. Chen, D. Wang, B. Z. Tang and Y. Liao, *ACS Nano*, 2023, **17**, 4601–4618.
9 H. Chen, S. Yan, L. Zhang, B. Zhao, C. Zhu, G. Deng and J. Liu, *Sens. Actuators, B*, 2024, **405**, 135346.
10 J. Liu, H. Chen, Y. Yang, Q. Wang, S. Zhang, B. Zhao, Z. Li, G. Yang and G. Deng, *Mater. Horiz.*, 2023, **10**, 3791–3796.
11 E. Thimsen, B. Sadtler and M. Y. Berezin, *Nanophotonics*, 2017, **6**, 1043–1054.
12 K.-W. Lee, Y. Gao, W.-C. Wei, J.-H. Tan, Y. Wan, Z. Feng, Y. Zhang, Y. Liu, X. Zheng, C. Cao, H. Chen, P. Wang, S. Li, K.-T. Wong and C.-S. Lee, *Adv. Mater.*, 2023, **35**, 2211632.
13 J. Guan, C. Liu, C. Ji, W. Zhang, Z. Fan, P. He, Q. Ouyang, M. Qin and M. Yin, *Small*, 2023, **19**, 2300203.
14 Y. Chu, X.-Q. Xu and Y. Wang, *J. Phys. Chem. Lett.*, 2022, **13**, 9564–9572.
15 Z. Zhang, Y. Du, X. Shi, K. Wang, Q. Qu, Q. Liang, X. Ma, K. He, C. Chi, J. Tang, B. Liu, J. Ji, J. Wang, J. Dong, Z. Hu and J. Tian, *Nat. Rev. Clin. Oncol.*, 2024, **21**, 449–467.
16 S. Roy, N. Bag, S. Bardhan, I. Hasan and B. Guo, *Adv. Drug Delivery Rev.*, 2023, **197**, 114821.
17 R. Ge, P. Yan, Y. Liu, Z. Li, S. Shen and Y. Yu, *Adv. Funct. Mater.*, 2023, **33**, 2301138.
18 X. Kong, J. Liang, M. Lu, K. Zhang, E. Zhao, X. Kang, G. Wang, Q. Yu, Z. Gan and X. Gu, *Adv. Mater.*, 2024, **36**, 2409041.
19 M. Shi, Z. Fu, W. Pan, K. Wang, X. Liu, N. Li and B. Z. Tang, *Adv. Healthcare Mater.*, 2024, **13**, 2303749.
20 Y. Chen, Y. Ran, Z. Rao, Q. Wang, J. Wang, Z. Liu, Q. Zhou, X. Lei, Z. Xu and J. Ming, *ACS Mater. Lett.*, 2024, **6**, 3915–3924.
21 M. Overchuk, R. A. Weersink, B. C. Wilson and G. Zheng, *ACS Nano*, 2023, **17**, 7979–8003.
22 C.-A. Shen, M. Stolte, J.-H. Kim, A. Rausch and F. Würthner, *J. Am. Chem. Soc.*, 2021, **143**, 11946–11950.
23 R. Englman and J. Jortner, *Mol. Phys.*, 1970, **18**, 145–164.
24 F. C. Spano and C. A. Silva, *Annu. Rev. Phys. Chem.*, 2014, **65**, 477–500.
25 Y. Wang, G. Xia, J. Wang, M. Wang, W. Guo, M. Tan, L. Si, Y. Yang, H. Wang and H. Wang, *Sci. China: Chem.*, 2023, **67**, 612–621.
26 X. Liu, Q. Qiao, W. Tian, W. Liu, J. Chen, M. J. Lang and Z. Xu, *J. Am. Chem. Soc.*, 2016, **138**, 6960–6963.
27 Z. Ye, W. Yang, C. Wang, Y. Zheng, W. Chi, X. Liu, Z. Huang, X. Li and Y. Xiao, *J. Am. Chem. Soc.*, 2019, **141**, 14491–14495.
28 J. Xu, M. Huang, H. Pang, Z. Weng, G. Hu, S. Zhang, Q. Yang and Q. Wu, *Aggregate*, 2024, **5**, e546.
29 Y. Li, T. Ma, H. Jiang, W. Li, D. Tian, J. Zhu and Z. Li, *Angew. Chem., Int. Ed.*, 2022, **61**, e202203093.
30 Y. Yang, C. Sun, S. Wang, K. Yan, M. Zhao, B. Wu and F. Zhang, *Angew. Chem., Int. Ed.*, 2022, **61**, e202117436.
31 B. Wang, H. Zhou, L. Chen, Y. Ding, X. Zhang, H. Chen, H. Liu, P. Li, Y. Chen, C. Yin and Q. Fan, *Angew. Chem., Int. Ed.*, 2024, **63**, e202408874.
32 G. Niu, X. Bi, Y. Kang, H. Zhao, R. Li, M. Ding, B. Zhou, Y. Zhai, X. Ji and Y. Chen, *Adv. Mater.*, 2024, **36**, 2407199.
33 D. Zhou, G. Zhang, J. Li, Z. Zhuang, P. Shen, X. Fu, L. Wang, J. Qian, A. Qin and B. Z. Tang, *ACS Nano*, 2024, **18**, 25144–25154.
34 Y. Dai, F. Zhang, K. Chen, Z. Sun, Z. Wang, Y. Xue, M. Li, Q. Fan, Q. Shen and Q. Zhao, *Small*, 2023, **19**, 2206053.
35 Z. Li, P.-Z. Liang, L. Xu, X. Zhang, K. Li, Q. Wu, X. Lou, T. Ren, L. Yuan and X. Zhang, *Nat. Commun.*, 2023, **14**, 1843.
36 X. Xie, Y. Dong, Y. Zhang, Z. Xie, X. Peng, Y. Huang, W. Yang, B. Li and Q. Zhang, *Bioact. Mater.*, 2024, **43**, 460–470.
37 M. Zhao, W. Lai, B. Li, T. Bai, C. Liu, Y. Lin, S. An, L. Guo, L. Li, J. Wang and F. Zhang, *Angew. Chem., Int. Ed.*, 2024, **63**, e202403968.
38 C. Ou, L. An, Z. Zhao, F. Gao, L. Zheng, C. Xu, K. Zhang, J. Shao, L. Xie and X. Dong, *Aggregate*, 2022, **4**, e290.
39 Y. Meng, J. Gao, P. Zhou, X. Qin, M. Tian, X. Wang, C. Zhou, K. Li, F. Huang and Y. Cao, *Angew. Chem., Int. Ed.*, 2024, **63**, e202318632.
40 F. Ma, Q. Jia, Z. Deng, B. Wang, S. Zhang, J. Jiang, G. Xing, Z. Wang, Z. Qiu, Z. Zhao and B. Z. Tang, *ACS Nano*, 2024, **18**, 9431–9442.
41 Y. Li, J. Zhuang, Y. Lu, N. Li, M. Gu, J. Xia, N. Zhao and B. Z. Tang, *ACS Nano*, 2021, **15**, 20453–20465.
42 X. Fan, Q. Xia, Y. Zhang, Y. Li, Z. Feng, J. Zhou, J. Qi, B. Z. Tang, J. Qian and H. Lin, *Adv. Healthcare Mater.*, 2021, **10**, 2101043.
43 M. Fan, X. Zheng, W. Cheng, H. Wei, P. Li, C. Ji and M. Yin, *Adv. Funct. Mater.*, 2024, **34**, 2402455.

44 C. Sun, B. Li, M. Zhao, S. Wang, Z. Lei, L. Lu, H. Zhang, L. Feng, C. Dou, D. Yin, H. Xu, Y. Cheng and F. Zhang, *J. Am. Chem. Soc.*, 2019, **141**, 19221–19225.
45 K. Wei, Y. Wu, X. Zheng, L. Ouyang, G. Ma, C. Ji and M. Yin, *Angew. Chem., Int. Ed.*, 2024, **63**, e202404395.
46 D. Gao, Z. Luo, Y. He, L. Yang, D. Hu, Y. Liang, H. Zheng, X. Liu and Z. Sheng, *Small*, 2023, **19**, 2206544.
47 C. Zhou, Z. Li, Z. Zhu, G. W. N. Chia, A. Mikhailovsky, R. J. Vázquez, S. J. W. Chan, K. Li, B. Liu and G. C. Bazan, *Adv. Mater.*, 2022, **34**, 2201989.
48 K. Liu, D. Hu, L. He, Z. Wang, P. Cheng, P. Sun, Y. Chen and D. Li, *J. Nanobiotechnol.*, 2024, **22**, 451.
49 P. Chen, F. Qu, S. Chen, J. Li, Q. Shen, P. Sun and Q. Fan, *Adv. Funct. Mater.*, 2022, **32**, 2208463.
50 C. Ayala-Orozco, D. Galvez-Aranda, A. Corona, J. M. Seminario, R. Rangel, J. N. Myers and J. M. Tour, *Nat. Chem.*, 2023, **16**, 456–465.
51 Y. Yadav, E. Owens, S. Nomura, T. Fukuda, Y. Baek, S. Kashiwagi, H. S. Choi and M. Henary, *J. Med. Chem.*, 2020, **63**, 9436–9445.
52 T. Fukuda, S. Yokomizo, S. Casa, H. Monaco, S. Manganiello, H. Wang, X. Lv, A. D. Ulumben, C. Yang, M. Kang, K. Inoue, M. Fukushi, T. Sumi, C. Wang, H. Kang, K. Bao, M. Henary, S. Kashiwagi and H. S. Choi, *Angew. Chem., Int. Ed.*, 2022, **61**, e202117330.
53 Y. Wang, G. Xia, M. Tan, M. Wang, Y. Li and H. Wang, *Adv. Funct. Mater.*, 2022, **32**, 2113098.
54 J. Park, Y. Choi, H. Chang, W. Um, J. H. Ryu and I. C. Kwon, *Theranostics*, 2019, **9**, 8073–8090.
55 H. Kang, S. Rho, W. R. Stiles, S. Hu, Y. Baek, D. W. Hwang, S. Kashiwagi, M. S. Kim and H. S. Choi, *Adv. Healthcare Mater.*, 2019, **9**, 1901223.
56 Y. Wang, Y. Li, Q. Yan, X. Liu, G. Xia, Q. Shao, K. Liang, L. Hong, B. Chi and H. Wang, *Dyes Pigm.*, 2020, **173**, 107977.